

## Understanding the nature of Pt-Rh synergy for three-way conversion catalysis



Yuejin Li<sup>a,\*</sup>, Ke-Bin Low<sup>b</sup>, Andreas Sundermann<sup>c</sup>, Haiyang Zhu<sup>b</sup>, Luis E. Betancourt<sup>b</sup>, Chansoon Kang<sup>b</sup>, Shantel Johnson<sup>b</sup>, Shaohua Xie<sup>d</sup>, Fudong Liu<sup>d</sup>

<sup>a</sup> BASF Environmental Catalyst and Metal Solutions, Iselin, NJ 08830, USA

<sup>b</sup> BASF Corporation, Iselin, NJ 08830, USA

<sup>c</sup> hte GmbH, Kurpfalzring 104, Heidelberg 69123, Germany

<sup>d</sup> Department of Civil, Environmental, and Construction Engineering, Catalysis Cluster for Renewable Energy and Chemical Transformations (REACT), NanoScience Technology Center (NSTC), University of Central Florida, Orlando, FL 32816, USA

### ARTICLE INFO

#### Keywords:

Pt-Rh synergy

TWC

Automotive catalysts

### ABSTRACT

A series of Al<sub>2</sub>O<sub>3</sub> supported Pt, Rh and Pt-Rh catalysts was investigated for TWC catalysis. Profound synergy between Pt and Rh was found on all Pt-Rh compositions relative to their single metal references with significantly reduced light-off temperatures. The nature of this synergy was probed using various characterization techniques. CO chemisorption, CO-DRIFTS and XPS results show that the surface Rh concentrations on aged Pt-Rh catalysts are much higher than that of the Rh reference. In addition, on the bimetallic catalysts the Rh species is in a more reduced state as indicated by XPS and XANES. AC-STEM/EDS results clearly illustrate that there are two types of Rh species on an aged Pt-Rh catalyst in terms of its location: one sitting on Pt particles as Rh nanoparticles and the other associated with the Al<sub>2</sub>O<sub>3</sub> support as sub-nano Rh moieties. The Pt-Rh bimetallic particles contain a certain degree of Pt-Rh alloy as evidenced by the upshift of the metal XRD peaks and the Pt-Rh coordination from the EXAFS measurement. All structural and microscopy analyses suggest that Rh is surface enriched on the Pt-Rh particles, and it is the surface enriched Rh species that plays a primary role in enhancing the activity of Pt-Rh catalysts.

### 1. Introduction

Owing to their high intrinsic activity in activating carbon monoxide (CO), hydrocarbons (HC) and nitrogen oxides (NO<sub>x</sub>) as well as their excellent hydrothermal stability, Pd and Rh are the main metal components in modern three-way conversion (TWC) catalysts [1]. Driven by the increasingly stringent emission regulations worldwide, currently more than 80% of the global Pd and Rh consumptions are for automotive catalysts. This has created a severe supply shortage for Pd and Rh over the past few years and drastically driven up their prices, especially for Rh. On the other hand, the price of Pt has been decreasing to about one half that of Pd. This situation has triggered intense activities in the industry to substitute a fraction of Pd by Pt and to reduce Rh usage in TWC catalysts [2].

The main challenge for employing Pt in TWC is its poor thermal stability under TWC aging conditions (950 – 1050 °C), resulting in severely sintering Pt particles [3–8]. In addition, Pt is intrinsically less

active for TWC than Pd and Rh at low temperatures, mainly due to the CO inhibition effect on Pt surfaces [9–11]. Rh, on the other hand, is very effective for TWC catalysis especially for NO<sub>x</sub> reduction [12]. Although Rh is more resistant to sintering, under high-temperature lean aging conditions Rh can be deactivated by forming inactive compounds with support, such as Rh aluminate [13–17], or migrating into the support [18]. Currently, Rh usages are already quite low in modern commercial TWC catalysts (< 0.1 g per vehicle) [1]. Further decreasing Rh loading would present a significant technical challenge.

One potential strategy for simultaneously improving Rh and Pt efficiencies in TWC catalysts is to create a mutually beneficial effect between Pt and Rh. Pt-Rh synergy for TWC and NO<sub>x</sub> reduction catalysis has been reported and debated in literature [9,19–24]. For example, Oh and Carpenter [19] reported a Pt-Rh/Al<sub>2</sub>O<sub>3</sub> catalyst (0.049 wt% Pt, 0.023 wt % Rh) made by sequential-impregnation, which showed a much lower light-off temperature for CO oxidation than the single metallic Pt and Rh catalysts after a mild aging at 700 – 850 °C in engine exhaust. However,

\* Corresponding author.

E-mail address: [yuejin.li@basf-catalystsmtals.com](mailto:yuejin.li@basf-catalystsmtals.com) (Y. Li).

they did not observe the same effect on a catalyst made by co-impregnation. Larkis et al. [22] investigated NO + H<sub>2</sub> and NO + CO reactions on a series of Al<sub>2</sub>O<sub>3</sub> supported Pt/Rh catalysts that were H<sub>2</sub>-reduced but not thermally aged. They observed a synergistic effect on 95Pt/5Rh/Al<sub>2</sub>O<sub>3</sub> (95 wt% Pt, 5 wt% Rh) for both reactions but not on 60Pt/40Rh. Hu et al. [20] investigated a set of monolithic TWC catalysts coated with Pt, Rh and Pt-Rh on Al<sub>2</sub>O<sub>3</sub> support and reported that the Pt-Rh catalyst had a strong synergistic effect after a simulated auto exhaust aging at 900 °C for 12 h. However, they did not observe any synergistic effect after a rich aging or on a fresh Pt-Rh catalyst.

Complete absence of Pt-Rh synergy was also reported [9,23,24]. For example, over a series SiO<sub>2</sub> supported Pt-Rh alloy catalysts (with 25, 50, 75 at% Rh) Pt-Rh synergy was not observed for CO oxidation and NO + CO reaction [9]. A Pt-Rh catalyst behaved like a simple combination of Pt and Rh as if they were separate individual components. The literature reports regarding Pt-Rh synergy are clearly not consistent. The inconsistency could be related to multiple reasons, such as catalyst composition (Pt/Rh ratio), catalyst preparation method, aging and evaluation conditions. In terms of Pt/Rh ratio, Larkis et al. argued that Pt-rich alloy is the necessary condition for the synergy. On a catalyst with comparable Pt and Rh loadings, such as 60Pt/40Rh, the catalyst contains both Pt-rich particles and Rh-rich particles and the overall kinetic effect is an average of synergistic effect (on Pt-rich particles) and non-synergistic effect (on Rh-rich particles) [22].

There are few studies on the origin of the Pt-Rh synergy, which remains poorly understood. Based on the XPS and microscopy results, Hu et al. concluded that the Rh species on the Pt-Rh/Al<sub>2</sub>O<sub>3</sub> catalyst was more readily reducible relative to that on Rh/Al<sub>2</sub>O<sub>3</sub>, which they believed to be key to reversing the deactivation of Rh caused by the formation of Rh aluminate after a lean aging [20]. This conclusion was supported by the work of Polvinen et al. [21]. On a Pt-Rh catalyst, aged at 1000 °C for 3 h in air, their XPS results indicated that there were two types of Rh species, one being reduction-resistant and the other readily reduceable. Further, using TEM/EDS they found Pt and Rh on all metal particles. To obtain insights into the origin of Pt-Rh synergy, one needs to understand the states and local structures of Rh and Pt on aged TWC catalysts. To this end, we have conducted a detailed study on a series of Al<sub>2</sub>O<sub>3</sub> supported Pt, Rh and Pt-Rh catalysts aged under various temperatures and feed environments. Here, we report profound synergistic effects between Pt and Rh for TWC catalysis over a wide range of Pt/Rh ratios. We have acquired a good understanding about the structural and electronic origin of the synergy by using a variety of characterization techniques, including CO chemisorption, SEM/EDS, TEM/EDS, AC-STEM/EDS, CO-DRIFTS, XPS, XRD, EXAFS and XANES.

## 2. Experimental section

### 2.1. Catalyst preparation

Pt (0.5, 1, 2 %), Rh (0.5 %) and Pt-Rh (0.5 % Pt-0.5 % Rh, 1 % Pt-0.5 % Rh, 2 % Pt-0.5 % Rh) catalysts were prepared by impregnating PGM precursors on a commercial  $\gamma$ -alumina support obtained from Sasol (BET surface area: 150 m<sup>2</sup>/g; pore volume: 1.1 cm<sup>3</sup>/g). Rh nitrate and Pt ethanalamine hydroxide were used as the metal precursors for Rh and Pt, respectively. For Pt-Rh bimetallic catalysts, Rh was impregnated on the support first, followed by Pt. Deionized water was added to an impregnated powder catalyst to form a slurry of ~30 % solid content, and the slurry pH was adjusted to 4–4.5 using nitric acid. The slurry was milled at 400 rpm for 10 min and then dried under stirring. The dried slurry was calcined at 550 °C for 2 h in air (fresh catalyst). The resulting material was crushed and sieved to 250–500  $\mu$ m fraction.

### 2.2. Catalyst performance evaluation

Before activity evaluation, all catalysts were aged at 1050 °C for 5 h with 10% H<sub>2</sub>O under an alternating lean/rich feed (10 min air/10 min 4

% H<sub>2</sub>/N<sub>2</sub>) in a flowing oven to simulate high-temperature engine aging conditions, such as the fuel-cut mode aging. After aging, the samples were cooled from 1050 to 400 °C in the lean feed (air with 10 % steam) and from 400 °C to room temperature in dry air. The aged catalysts were evaluated in a high throughput powder screening reactor using 100-mg sample (diluted to 1 mL with corundum) and with a total flow rate of 1.16 L/min, which is equivalent to a monolith gas hourly space velocity (GHSV) of 70,000 h<sup>-1</sup> (assuming 100 g/L washcoat loading). Two consecutive light-off runs were performed with a  $\lambda = 1$  oscillating feed ( $\lambda = 0.95/1.05$  cycled at 0.5 Hz) from 175 to 450 °C. The lean feed ( $\lambda = 1.05$ ) consisted of 0.7 % CO, 0.22 % H<sub>2</sub>, 3000 ppm HC (C1) (propene/propane = 2:1), 1500 ppm NO, 14 % CO<sub>2</sub>, 10 % H<sub>2</sub>O and ~1.8 % O<sub>2</sub>. The rich feed ( $\lambda = 0.95$ ) included 2.33 % CO, 0.77 % H<sub>2</sub>, 3000 ppm HC (C1), 1500 ppm NO, 14 % CO<sub>2</sub>, 10 % H<sub>2</sub>O and ~0.7 % O<sub>2</sub>. The exact lambda values were fine-tuned by adjusting the O<sub>2</sub> level based on an upstream  $\lambda$ -sensor. The first light-off run was used to stabilize catalyst performance (or de-greening), and the second light-off data were used for activity comparison. The concentrations of carbon monoxide (CO), nitric oxide (NO) and total hydrocarbon (HC) were continuously measured after catalysts, and inlet concentrations were monitored by repeated measurements via a bypass. Measurements were performed with gas analyzers of the ABB advance optima (AO2000) series. The conversion of a component (CO, NO or HC) is calculated as the percent of disappearance, i.e., Conversion = (Inlet concentration – Outlet concentration)/Inlet concentration x 100 %. Catalyst activity is also characterized by catalyst light-off temperature, which is defined as the temperature required to achieve 50 % conversion in a conversion – temperature plot. Light-off temperature is denoted as T<sub>50</sub>. Light-off temperatures for CO, NO and HC are expressed as CO T<sub>50</sub>, NO T<sub>50</sub> and HC T<sub>50</sub>, respectively (for further details on the experimental setup cf. [25]).

### 2.3. Catalyst characterization

CO chemisorption measurements were performed using a Quantachrome Autosorb-iQ instrument by titrating a reduced catalyst with multiple CO pulses (5% CO/He) at 20 °C. Before measurement, a sample was first pretreated with flowing He from room temperature to 150 °C at a ramp rate of 5 °C/min and holding at 150 °C for 10 min. The system was then purged with 10 % H<sub>2</sub>/Ar, ramped to 400 °C at 5 °C/min, and kept at 400 °C for 30 min. Finally, the system was switched to He again, holding the temperature at 400 °C for 15 min, then cooling to 35 °C at 20 °C/min, and holding at 20 °C for 30 min.

Three microscopy tools were applied to various samples. Scanning electron microscopy (SEM) was performed on aged 2% Pt and 2% Pt-0.5% Rh catalysts using field emission scanning microscopes from Thermo Fisher Scientific (Apreo and JEOL JSM-7800 F) with an acceleration voltage of 10.0 kV and beam current of 0.8 nA. Bruker XFlash 6130 Energy Dispersive X-ray Spectroscopy (EDS) was used to collect element maps to identify Pt and Pt/Rh particles. Unattended data acquisition technique was used using Bruker ESPRIT 2.1 software for efficient data collection for both imaging and EDS mapping. To avoid double counting, no overlap was allowed among neighboring images. One hundred images per sample were analyzed (imaging and EDS mapping) to enhance the statistic relevance. Scanning transmission electron microscopy (STEM) coupled with EDS was performed on aged 0.5% Rh catalyst using JEOL JEM-F200 S/TEM at 200 kV with dual 100 mm<sup>2</sup> silicon drift detectors (SDDs). The total X-ray collection solid angle was ~ 1.7 Sr. The sample was excited with a probe current of 180 pA. The minimum Rh size detection for this instrument ranges between 0.5 and 1.0 nm (depending on support thickness). Aberration corrected scanning transmission electron microscopy (AC-STEM) was performed on 2% Pt-0.5% Rh samples. The high-angle annular dark-field (HAADF) images were collected using the JEOL JEM-ARM200CF probe-corrected cold-field emission scanning transmission electron microscope operating at 200 kV. The electron probe employed for imaging had a nominal size of 0.1 nm with about 35 pA current. The camera length for the

HAADF detector was 6 cm, collecting signals between the semi-angles of 90 and 370 mrad.

For X-ray diffraction (XRD) experiment, powder samples were ground using a mortar and pestle and then packed onto a low background slide for analysis. A PANalytical MPD X'Pert Pro diffraction system was used to collect data in Bragg-Brentano geometry.  $\text{CuK}\alpha$  radiation was used in the analysis with generator settings of 45 kV and 40 mA. The optical path consisted of a  $1/4^\circ$  divergence slit, 0.04 radian soller slits, 15 mm mask,  $1/2^\circ$  anti-scatter slit,  $1/4^\circ$  anti-scatter slit, 0.04 radian soller slits, Ni filter, and X'Celerator linear position sensitive detector. Data were collected from  $10^\circ$  to  $90^\circ$  2 $\theta$  using a step size of  $0.026^\circ$  and a count time of 600 s per step. On samples showing Pt or Pt/Rh peaks, a secondary scan was collected from  $79^\circ$  to  $83^\circ$  2 $\theta$  using a step size of  $0.0066^\circ$  and a count time of 1000 s per step. Jade Plus 9 analytical X-ray diffraction software was used for phase identification and alloy determination.

X-ray photoelectron spectroscopy (XPS) experiments were conducted on a set of  $\text{Al}_2\text{O}_3$  supported catalysts (1 % Pt, 2 % Pt, 0.5 % Rh, 1 % Pt-0.5 % Rh and 2 % Pt-0.5 % Rh). Surface concentrations and oxidation states of metal species were probed using a Thermo Scientific NEXSA G2 X-ray Photoelectron Spectrometer with an Al K- $\alpha$  X-Ray source and Ar-flood gun. A ground powder sample with approximately 400 nm spot size was pressed onto indium tin oxide foil and loaded into the analysis chamber under high vacuum ( $1 \times 10^{-9}$  mbar). Data were processed and fitted using CasaXPS software with Gaussian-Lorentzian functions. Binding energy was calibrated using adventitious carbon (C 1s) at 284.8 eV. A survey scan at a pass energy of 160 eV was used to quantify all elements. Spectra for chemical speciation was performed by scanning the region 10 times with a pass energy of 35 eV at 0.06 s dwell time. Quantifications of chemical species were obtained by averaging the values from three measurements of the same sample.

Diffuse reflectance infrared Fourier transform spectroscopy with CO adsorption (CO-DRIFTS) was carried out on a Thermo iS50 infrared spectrometer equipped with a Harrick high temperature environmental chamber. A sample was ground to fine powder with a mortar and pestle and packed into a sample cup. The sample was reduced at  $400^\circ\text{C}$  in flowing 3 %  $\text{H}_2/\text{He}$  for 1 h and then cooled to  $30^\circ\text{C}$ . A spectrum was recorded as background prior to CO adsorption. CO adsorption was carried out at  $30^\circ\text{C}$  with a flow rate of 40 mL/min. IR spectra were recorded with CO exposure time up to 30 min. Then the sample was purged by flowing Ar to remove the gaseous CO in the chamber. IR spectrum was recorded on the sample with adsorbed CO. The difference spectrum between the sample with CO adsorption and background was used to characterize adsorbed CO species on the sample.

X-ray absorption spectroscopy (XAS) was measured at the 7-BM QAS beamline of the National Synchrotron Light Source II (NSLS-II) at Brookhaven National Laboratory. X-ray absorption near edge structure (XANES) and extended X-ray absorption fine structure (EXAFS) of Pt L<sub>3</sub>-edge and Rh K-edge were measured in fluorescence mode and processed using Athena and Artemis from the Demeter software package. Pt foil and Rh foil were used for energy calibrations and monochromator drift corrections, respectively. The processed EXAFS  $\chi(k)$  was weighted by  $k^2$  to amplify the high- $k$  oscillations. For Fourier-transformed (FT) spectra, the  $k$  range between 3.0 and 12.0 Å was used for Pt L<sub>3</sub>-edge and the  $k$  range between 3.0 and 11.0 Å was used for Rh K-edge.

### 3. Results and discussion

#### 3.1. Catalytic performance

**Fig. 1** shows the CO, NO and HC conversions as a function of temperature on seven PGM compositions (0.5 % Pt, 1 % Pt, 2 % Pt, 0.5 % Rh, 0.5 % Pt-0.5 % Rh, 1 % Pt-0.5 % Rh, and 2 % Pt-0.5 % Rh), and **Table 1** lists their corresponding T50s. Pt catalysts are least active (with the highest T50s) for all three conversions. The 0.5 % Rh catalyst shows much higher activities than the 2 % Pt catalyst; the difference between 2

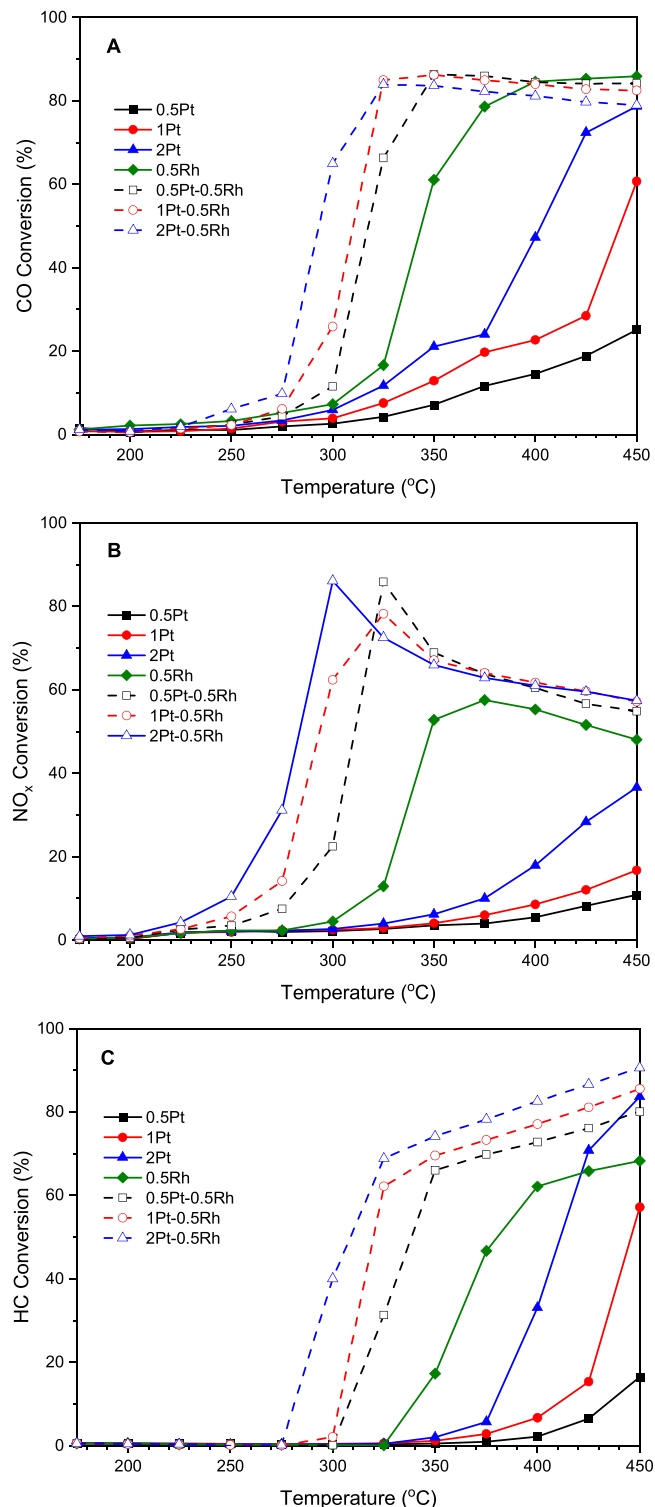


**Fig. 1.** Conversions of CO (A),  $\text{NO}_x$  (B) and HC (C) as a function of temperature over aged Pt, Rh and Pt-Rh catalysts. The number before Pt or Rh denotes its metal loading in weight percent.

% Pt and 0.5 % Rh in T50 is 58, > 100, and 29 °C for CO, NO and HC, respectively. Interestingly, when Pt and Rh are combined, the activity is significantly higher than the sum of Pt and Rh. For example, at  $325^\circ\text{C}$  the HC conversion is 68 % on 2 % Pt-0.5 % Rh, while the conversion is zero for either 0.5 % Rh or 2 % Pt. We can use  $\Delta\text{T50}$ , defined as  $\text{T50}_{\text{Rh}} - \text{T50}_{\text{Pt-Rh}}$ , to represent the improvement of a Pt-Rh catalyst over the Rh reference.  $\Delta\text{T50}$  was found to be proportional to the Pt loading in a Pt-

**Table 1**

Light-off temperatures ( $T_{50}$ ) and temperatures required for a TOF ( $T_{TOF}$ ) for Pt, Rh and Pt-Rh catalysts.

Catalyst	$T_{50}$ (°C) <sup>1</sup>			$T_{TOF}$ (°C) <sup>2</sup>		
	CO	NO <sub>x</sub>	HC	CO TOF = 10/s	NO <sub>x</sub> TOF = 0.6/s	HC TOF = 1/s
0.5Pt	-3	-3	-3	NA <sup>4</sup>	NA <sup>4</sup>	NA <sup>4</sup>
1Pt	442	-3	446	310	333	373
2Pt	403	-3	411	312	339	367
0.5Rh	345	353	382	300	300	330
0.5Pt- 0.5Rh	318	311	339	NA <sup>4</sup>	NA <sup>4</sup>	NA <sup>4</sup>
1Pt-0.5Rh	310	295	322	292	267	303
2Pt-0.5Rh	294	283	309	282	256	283

<sup>a</sup>  $T_{50}$  is the temperature required to reach 50% conversion;

<sup>b</sup>  $T_{TOF}$  is the temperature required to achieve a certain turnover frequency (TOF), which was calculated using conversion values below 10 % from Fig. 1 and the chemisorption data shown in Table 2, assuming 1:1 CO/metal stoichiometry;

<sup>c</sup> Conversion did not reach 50 % by 450 °C;

<sup>d</sup> Chemisorption data are not available.

### Rh catalyst.

In addition to light-off improvement, the Pt-Rh catalysts also substantially increased the high-temperature HC activity over the Rh reference. The high-temperature performance is further illustrated by a  $\lambda$ -sweep test at 350 °C (Fig. S1), where the average lambda value changed from lean (1.05) to rich (0.96). Throughout the lambda range, higher HC conversions were consistently observed on the Pt-Rh catalysts over the Rh reference. The light-off tests shown in Fig. 1 were conducted with a  $\lambda = 1$  oscillating feed ( $\lambda = 0.95/1.05$  cycled at 1 Hz). To understand the influence of feed condition, we also evaluated all catalysts using a  $\lambda = 1$  feed with a smaller oscillation amplitude ( $\lambda = 0.98/1.02$ ) and a constant  $\lambda = 1$  feed (Fig. S2). With all feed and test conditions, the Pt-Rh synergistic effect was confirmed. The kinetic effect of Pt-Rh synergy can also be illustrated by comparing a Pt-Rh catalyst with a Rh-only catalyst of higher Rh loading. As shown in Fig. S3, 1Pt-0.25Rh (1 % Pt, 0.25 % Rh) is significantly more active than 0.5Rh (0.5 % Rh); its  $T_{50}$ s are 29, 51 and 48 °C lower than 0.5Rh for CO, NO and HC, respectively. This clearly indicates that the Rh on a Pt-Rh/Al<sub>2</sub>O<sub>3</sub> catalyst is much more active than the Rh on Rh/Al<sub>2</sub>O<sub>3</sub>.

Table 1 also compares the TWC activities of the catalysts on a per-site basis in the form of temperature required to reach a certain turnover frequency or  $T_{TOF}$ . The  $T_{TOFs}$  for the two Pt catalysts (1Pt and 2Pt) are about the same, which are significantly higher than that of 0.5Rh, especially for NO and HC. On the other hand, the  $T_{TOFs}$  of the Pt-Rh catalysts are significantly lower than that of 0.5Rh. Overall,  $T_{TOF}$  follows the ranking, 2Pt-0.5Rh < 1Pt-0.5Rh < 0.5Rh < 2Pt = 1Pt, suggesting that at least some of the active sites on Pt-Rh catalysts are different from those of Pt and Rh monometallic catalysts. Thus, the Pt-Rh synergy for TWC catalysis have been unequivocally demonstrated not only in terms of overall conversion but also in TOF.

### 3.2. Catalyst characterization

CO chemisorption results on five Pt, Rh and Pt-Rh samples are summarized in Table 2. The amounts of CO adsorbed ( $\mu\text{mol/g}$ ) on the two bimetallic catalysts, 1Pt-0.5Rh and 2Pt-0.5Rh, are higher than the sums of their corresponding single component references by 52 % and 62 %, respectively. The calculated metal dispersions, based on 1:1 CO/metal stoichiometry, are undoubtedly higher on the bimetallic catalysts than their single metal references. This suggests that Pt and Rh are not completely isolated on the support and there is a mutual influence between the two metals.

The amounts of CO adsorption measured (or calculated metal dispersions) on the aged catalysts in general are very low. For Pt catalysts, the low metal dispersion is due to metal sintering after 1050 °C aging. For Rh, metal sintering on alumina is less a problem, but high-

**Table 2**

Summary of CO chemisorption and XPS results of aged catalysts.

Catalyst	CO chemisorption		XPS surface concentration and oxidation state			
	CO ads. ( $\mu\text{mol}/\text{g}_{\text{cat}}$ )	CO/Me <sup>a</sup> mol. ratio	Pt conc. (at%)	Pt <sup>0</sup> / Pt <sup>2+</sup> Ratio	Rh conc. (at%)	Rh <sup>0</sup> / Rh <sup>3+</sup> Ratio
1Pt	0.70	0.014	0.03	2.0		
2Pt	1.12	0.011	0.05	2.0		
0.5Rh	0.96	0.020			0.07	0.30
1Pt- 0.5Rh	2.52	0.025	0.03	0.85	0.10	0.32
2Pt- 0.5Rh	3.37	0.022	0.07	0.75	0.17	0.42

<sup>a</sup> Me is the total metal content in a sample, including both Pt and Rh on a bimetallic catalyst.

temperature aging in an oxidizing environment could cause Rh to lose its catalytic activity and ability to adsorb CO by forming an inactive compound with the alumina support. To understand the physical states of Pt and Rh on a Pt-Rh catalyst, we conducted a detailed analysis of aged 2Pt-0.5Rh/Al<sub>2</sub>O<sub>3</sub> catalyst as well as the single component Pt and Rh catalysts using SEM, TEM/EDS and AC-STEM/EDS.

To obtain particle size distributions for Pt and Pt-Rh, we conducted an extensive SEM/EDS analysis on aged 2Pt and 2Pt-0.5Rh catalysts by analyzing 894 and 1984 metal particles, respectively. Fig. 2 illustrates representative SEM images of aged 2Pt and 2Pt-0.5Rh catalysts and their particle size distributions. Most of Pt particles on 2Pt have diameters between 100 and 200 nm with an extensive tailing beyond 300 nm. The mean equivalent diameter for Pt particles is 179 nm. The particles on 2Pt-0.5Rh are visually smaller. The size histogram shows that the center of the distribution has shifted to about 100 nm with the mean equivalent diameter of 153 nm. STEM/EDS analysis was performed on the aged 0.5Rh/Al<sub>2</sub>O<sub>3</sub> catalyst to obtain information on the physical state of Rh. From all the TEM images collected, we could not identify any Rh particle (Fig. 3). Based on the instrument limitation and our investigation on a control sample (2 % Rh/Al<sub>2</sub>O<sub>3</sub> calcined at 850 °C), we may conclude that Rh particles, if exist, must be smaller than 0.5 nm. Area EDS scans of several locations on the sample clearly indicate that Rh species is well dispersed on the Al<sub>2</sub>O<sub>3</sub> support despite 1050 °C aging. Therefore, the metal particles detected by SEM on 2Pt-0.5Rh are all Pt-containing particles. Based on the microscopy results, we may conclude that the presence of Rh on 2Pt-0.5Rh inhibits the sintering of Pt particles during aging.

The local structure of aged 2Pt-0.5Rh catalyst was further examined in detail using AC-STEM in HAADF and LAADF views coupled with both spot and area EDS. Fig. 4 shows the images and element maps of two typical metal particles found on the aged 2Pt-0.5Rh sample. The metal particles are unequivocally bimetallic in nature, which consist of two distinct compositional regions, a Pt-rich majority and Rh-rich islands. EDS spot analyses of 4 particles show varied Rh compositions (4–17 mol %) in the Pt-rich region and 60–80 mol % Rh on the Rh-rich islands. Given that the overall Rh composition on 2Pt-0.5Rh is 32 mol%, a significant fraction of Rh appears to be associated with the Pt particles.

In addition to the large metallic particles, we also performed EDS scans in areas free of obvious nanoparticles. Shown in Fig. 5 are AC-STEM images and EDS spectra of 4 selected areas. There appear to be some small metal clusters or even single atoms within the highlighted areas, and some of the bright spots seem to be entrenched into the support lattice. The EDS spectra confirm that Rh and Pt are indeed present in these areas. In some areas, higher Rh intensity was observed relative to Pt (for example, EDS3 and EDS4 in Fig. 5). Based on the microscopy experiments, we can conclude that there exist two types of Rh species on the aged 2Pt-0.5Rh/Al<sub>2</sub>O<sub>3</sub> catalyst in terms of its location, one that decorates large Pt particles (as highly dispersed Rh species or island) and the other closely associated with the Al<sub>2</sub>O<sub>3</sub> support as sub-

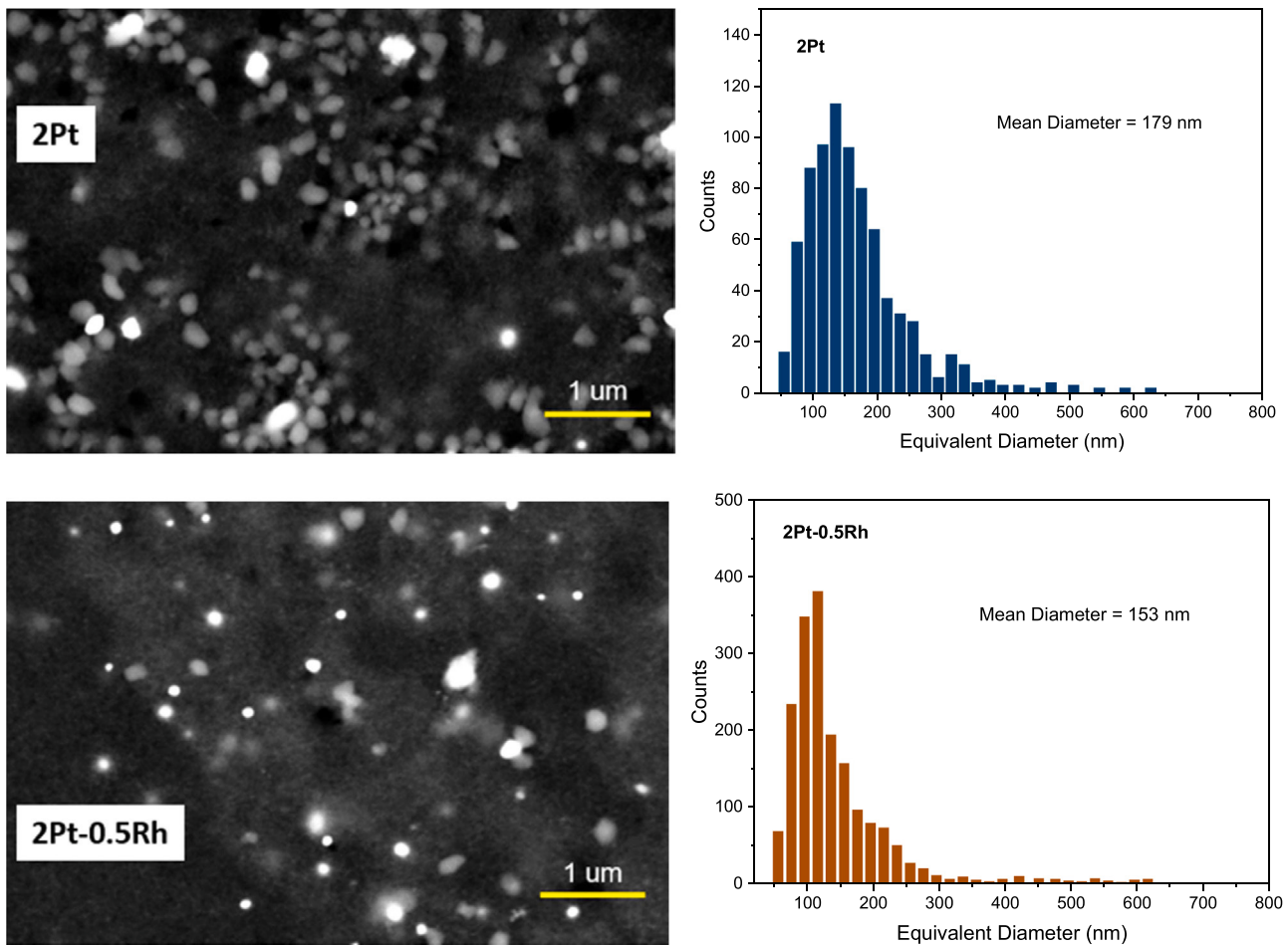


**Fig. 2.** Representative SEM images and PGM particle size histograms for 2Pt (2 % Pt on  $\text{Al}_2\text{O}_3$ ) and 2Pt-0.5Rh (2 % Pt – 0.5 % Rh on  $\text{Al}_2\text{O}_3$ ) catalysts. Both catalysts were aged at 1050 °C for 5 h with 10 %  $\text{H}_2\text{O}$  in a lean/rich alternating feed. The histograms were generated by analyzing 894 particles for 2Pt and 1984 particles for 2Pt-0.5Rh, and each particle was confirmed to be a PGM particle by EDS analysis.

nanometer Rh species.

To understand the effect of aging on the formation of bimetallic particles and local composition change, we also performed AC-STEM analysis on a fresh 2Pt-0.5Rh catalyst (calcined at 550 °C for 2 h in air). As shown in Fig. 6, Pt is highly dispersed as particles mostly < 2 nm, and Rh is detected (by area EDS) on each of the Pt particles with an average Rh content of 25 mol%. The overall Rh content on the catalyst is 32 mol%, and thus over 70 % Rh on the catalyst is associated with the Pt particles. This clearly demonstrates that the affinity between Pt and Rh does not require a high-temperature exposure.

Fig. 7 shows XRD scans of fresh and aged 0.5Rh, 2Pt and 2Pt-0.5Rh catalysts. Upon aging, the  $\gamma\text{-}\text{Al}_2\text{O}_3$  phase was converted to  $\theta\text{-}\text{Al}_2\text{O}_3$  and  $\delta\text{-}\text{Al}_2\text{O}_3$  with increased peak intensity. Most of the Pt or Pt/Rh diffraction peaks overlap with the strong  $\text{Al}_2\text{O}_3$  peaks, except for the one between 81 and 82°  $2\theta$ , and this peak is used to identify Pt particles or Pt/Rh alloy formation. On both fresh and aged 0.5Rh catalysts, no Rh peak is detected (Fig. 7B). On fresh 2Pt and 2Pt-0.5Rh catalysts, a weak, broad peak appears at the same position around 81.3°, which is attributed to Pt (311) diffraction. The intensity of this peak is significantly higher on aged 2Pt, but its position remains same. This peak is upshifted by 0.34° on aged 2Pt-0.5Rh, indicating the formation of Pt-Rh alloy, and the alloy phase is estimated to contain 91 mol% Pt and 9 mol% Rh.

The surface PGM concentrations and their oxidation states of five aged catalysts (1Pt, 2Pt, 0.5Rh, 1Pt-0.5Rh and 2Pt-0.5Rh) were analyzed by XPS. Fig. 8 shows the Pt 4f and Rh 3d spectra of these samples. Due to a strong overlap between Al 2p and the Pt 4f peaks and a slight overlap between Rh 3d and Pt 3d peaks, peak deconvolution was performed to

quantify different oxidation states of PGM species. The surface concentrations of Pt and Rh were calculated by normalizing their PGM quantity (area) over the sum of all XPS detected species. Table 2 summarizes the surface concentrations and oxidation states of Pt and Rh on these catalysts. In general, Pt surface concentrations on all samples are very low relative to their metal loading, which is consistent with the CO chemisorption measurements (Table 2) and is obviously due to severe Pt sintering during aging (Fig. 2). Identical Pt concentrations were detected on 1Pt and 1Pt-0.5Rh. However, the Pt concentration is higher on 2Pt-0.5Rh (0.07 mol%) than 2Pt (0.05 mol%). The surface oxidation states of Pt on the Pt-only references are dominated by  $\text{Pt}^0$  (about 2/3). Interestingly, on the Pt-Rh catalysts, the Pt surface tends to be more oxidized (<50%  $\text{Pt}^0$ ).

For Rh-containing catalysts, the Rh surface concentration is noticeably higher on Pt-Rh catalysts than on the Rh reference and is proportional to Pt loading. Given the identical Rh loading on these samples (0.5 wt%), this clearly suggests that the presence of Pt increases the XPS detectable surface Rh concentration. The oxidation states of Rh on these catalysts are dominated by  $\text{Rh}^{3+}$  (as  $\text{Rh}_2\text{O}_3$ ). Contrary to the effect of Rh on Pt oxidation state, the presence of Pt tends to make Rh more reduced ( $\text{Rh}^0/\text{Rh}^{3+} = 0.30$  on 0.5Rh vs. 0.42 on 2Pt-0.5Rh). Since Rh species can be located on Pt particles and on the  $\text{Al}_2\text{O}_3$  support (AC-STEM results), it is thus reasonable to deduce that the more reduced Rh should come from the Rh species located on the Pt particles. The mutual influence in oxidation state between Pt and Rh is a further confirmation of the physical origin of Pt-Rh synergy.

The surface characteristics of five aged Pt, Rh and Pt-Rh catalysts

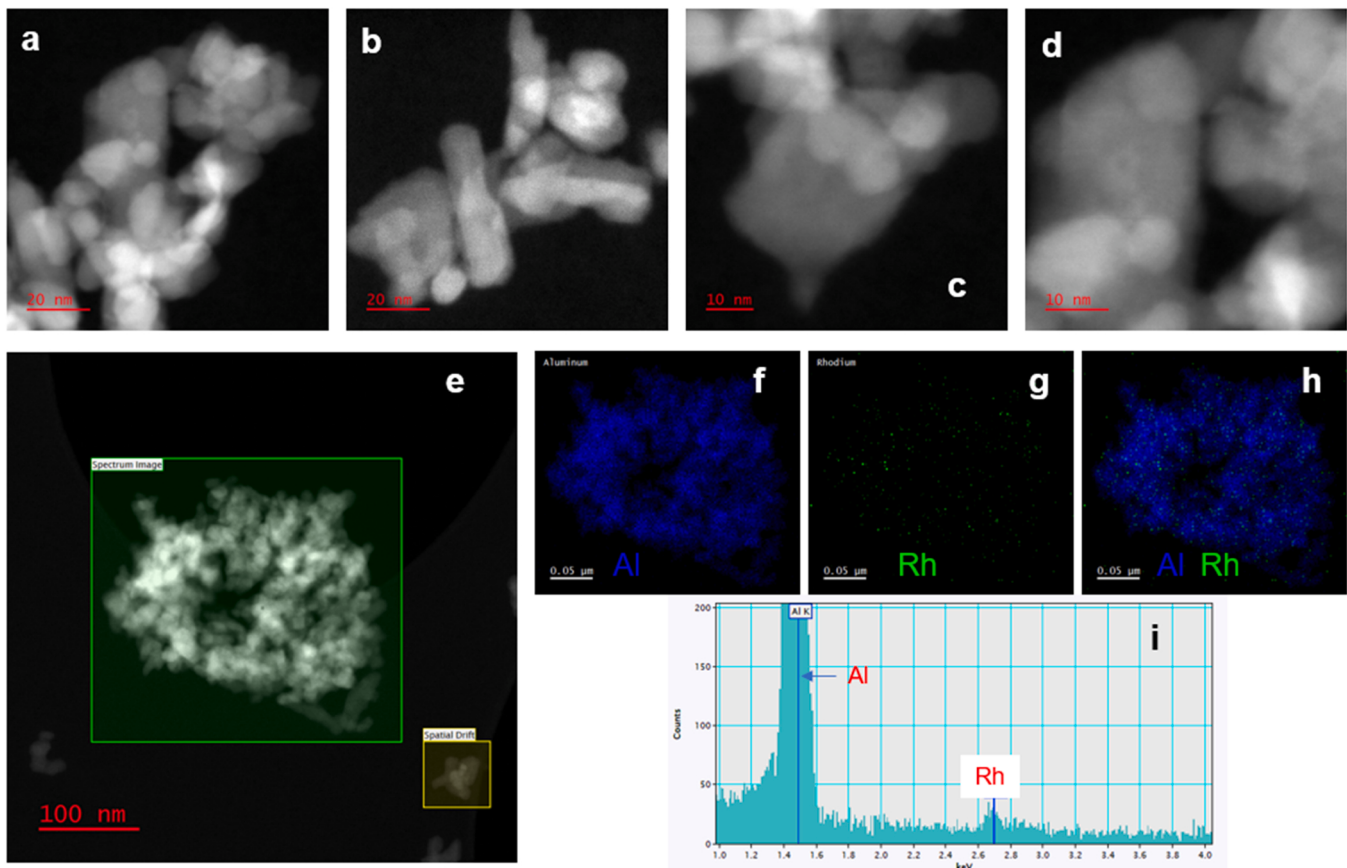


**Fig. 3.** TEM images of aged 0.5% Rh/Al<sub>2</sub>O<sub>3</sub> catalyst (a-e) as well as element mapping (f-h) and EDS area spectrum (i) of highlighted area in graph e. This sample was aged at 1050 °C for 5 h with 10% H<sub>2</sub>O in a lean/rich alternating feed.

were also examined using CO-DRIFTS after a reduction treatment at 400 °C. As shown in Fig. 9, the intensities of CO adsorption at 2061 cm<sup>-1</sup> (CO adsorbed on metallic Pt) on the two Pt catalysts are extremely low, a consequence of their low Pt dispersion (~1%). On the Rh reference and two Pt-Rh catalysts, a pair of CO adsorption bands were observed, and they are assigned to the symmetrical and asymmetrical stretching vibration of a dicarbonyl complex on Rh<sup>+</sup>. Upon close examination of the dicarbonyl bands, there appear to be two pairs of peaks (2095 and 2023; 2087 and 2015 cm<sup>-1</sup>), they are likely the results of CO adsorbed on two different types of Rh sites. Interestingly, the intensity of the CO adsorption on the Rh sites is clearly proportional to the Pt content in the Pt-Rh catalysts, i.e., the presence of Pt profoundly increases the number of surface Rh sites that are capable of adsorbing CO. This finding is entirely consistent with the CO chemisorption measurement and the XPS results. Further, a weak, broad CO adsorption band was observed around 1825 cm<sup>-1</sup> on 1Pt-0.5Rh and 2Pt-0.5Rh but not on 0.5Rh, 1Pt or 2Pt. This band can be assigned to bridge-bonded CO adsorption on Rh<sup>0</sup>, suggesting that Rh is more readily reduceable on Pt-Rh than on the Rh-only reference.

X-ray absorption spectroscopy (XAS) was used to measure the structures and valent states of Pt and Rh on five aged catalysts (1Pt, 2Pt, 0.5Rh, 1Pt-0.5Rh and 2Pt-0.5Rh). Fig. 10A shows the normalized Pt L<sub>3</sub>-edge XANES for Pt foil, PtO<sub>2</sub> and the Pt-containing catalysts. The XANES spectra for all Pt-containing catalysts are almost identical to that for Pt foil, implying that the Pt species on all aged catalysts are close to metallic Pt. The average oxidation states of Pt obtained by linear combination fitting for Pt L<sub>3</sub>-edge XANES are shown in Fig. S8 and Table S1. For a given Pt loading, the average oxidation states of Pt on Pt and Pt-Rh catalysts are identical (0.16 and 0.17 for 1Pt/Al<sub>2</sub>O<sub>3</sub> and 1Pt-0.5Rh, respectively; 0.12 and 0.10 for 2Pt/Al<sub>2</sub>O<sub>3</sub> and 2Pt-0.5Rh/Al<sub>2</sub>O<sub>3</sub>,

respectively) within experimental error ( $\pm 0.01$ ). The EXAFS results (Fig. 10B and S9) show typical peaks located at ca. 2.50–2.76 Å that could be assigned to Pt-Pt coordination shell in Pt foil, 1Pt/Al<sub>2</sub>O<sub>3</sub>, and 2Pt/Al<sub>2</sub>O<sub>3</sub>. However, on 1Pt-0.5Rh/Al<sub>2</sub>O<sub>3</sub> and 2Pt-0.5Rh/Al<sub>2</sub>O<sub>3</sub> peaks with different relative intensities and sub-peak ratios were observed, indicating the possible presence of Pt-Rh coordination besides Pt-Pt coordination within these samples. To better understand the difference in Pt coordination structures, the EXAFS fitting results for Pt L<sub>3</sub>-edge are shown in Table S2. The coordination numbers (CNs) of Pt-Pt bond for 1Pt/Al<sub>2</sub>O<sub>3</sub> (11.5) and 2Pt/Al<sub>2</sub>O<sub>3</sub> (11.4) are similar and slightly lower than that for Pt foil (12.0) but higher than those for 1Pt-0.5Rh/Al<sub>2</sub>O<sub>3</sub> (10.8) and 2Pt-0.5Rh/Al<sub>2</sub>O<sub>3</sub> (10.4). At the same time, similar CNs of Pt-Rh bond were observed for 1Pt-0.5Rh/Al<sub>2</sub>O<sub>3</sub> (0.7) and 2Pt-0.5Rh/Al<sub>2</sub>O<sub>3</sub> (0.7) catalysts. The EXAFS curve fitting results suggest that a part of Pt is coordinated with Rh on 1Pt-0.5Rh/Al<sub>2</sub>O<sub>3</sub> and 2Pt-0.5Rh/Al<sub>2</sub>O<sub>3</sub>.

The XANES and EXAFS of Rh K-edge were collected on 0.5Rh/Al<sub>2</sub>O<sub>3</sub>, 1Pt-0.5Rh/Al<sub>2</sub>O<sub>3</sub>, and 2Pt-0.5Rh/Al<sub>2</sub>O<sub>3</sub>. As shown in Fig. 11A, the XANES spectra for all Rh-containing catalysts are similar and close to that for Rh<sub>2</sub>O<sub>3</sub> reference. Upon close examination (inserted graph in Fig. 11A), we find that the white line intensity is inversely proportional to Pt loading, indicating that the presence of Pt decreases the average oxidation state of Rh. This trend is confirmed and quantified by the linear combination of the fitting results for Rh K-edge XANES (Fig. S10 and Table S3), showing that the average oxidation state of Rh decreases in the order of 0.5Rh/Al<sub>2</sub>O<sub>3</sub> (2.86) > 1Pt-0.5Rh/Al<sub>2</sub>O<sub>3</sub> (2.67) > 2Pt-0.5Rh/Al<sub>2</sub>O<sub>3</sub> (2.45). The EXAFS results (Fig. 11B and S11) show that the Rh-O and Rh-O-Al coordination shells are present in 0.5Rh/Al<sub>2</sub>O<sub>3</sub>. In addition to the Rh-O and Rh-O-Al coordination shells, the Rh-Pt coordination shell is likely present in 1Pt-0.5Rh/Al<sub>2</sub>O<sub>3</sub> and 2Pt-0.5Rh/Al<sub>2</sub>O<sub>3</sub>.

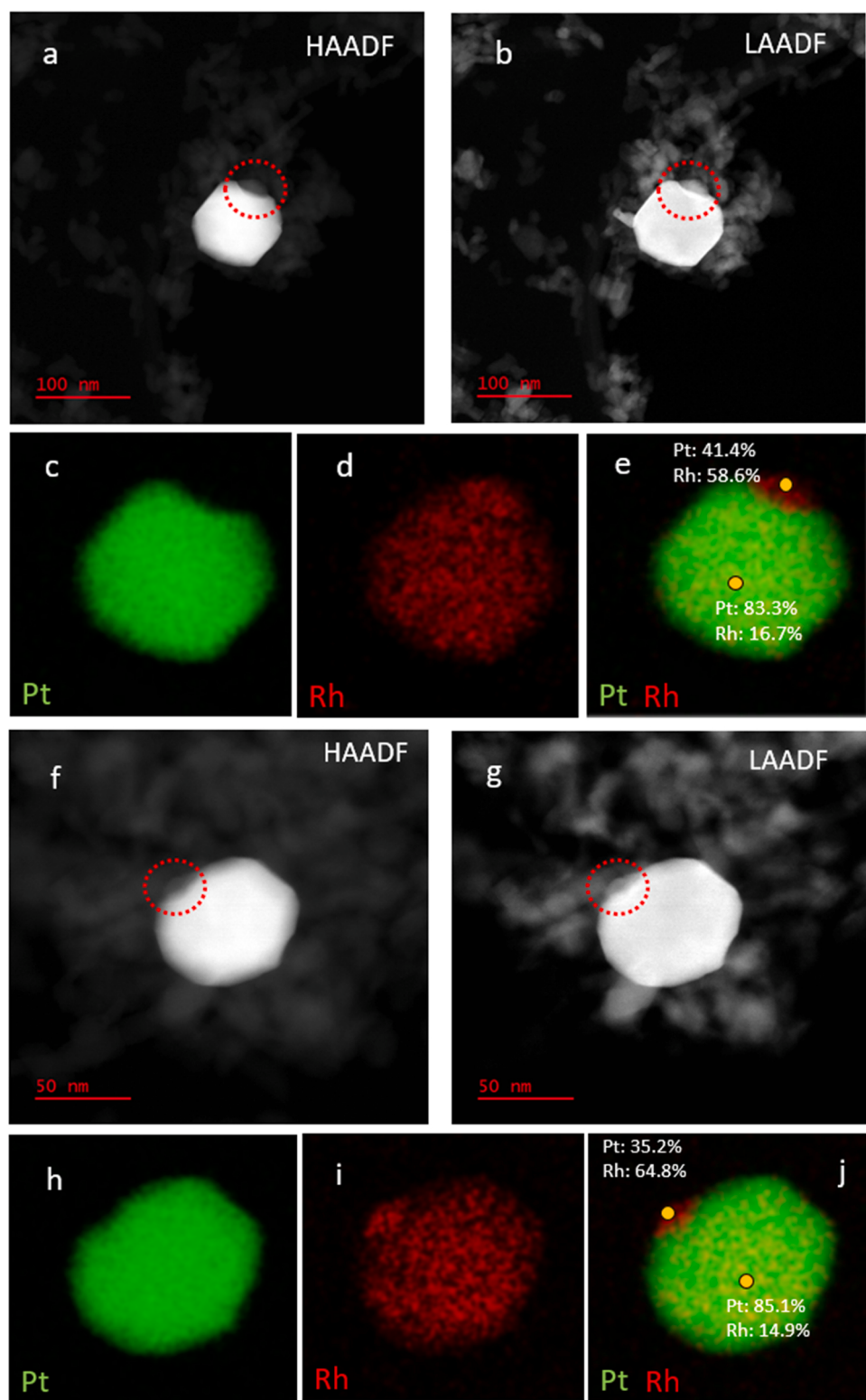


**Fig. 4.** AC-STEM images of Pt/Rh particles on aged 2Pt-0.5Rh/Al<sub>2</sub>O<sub>3</sub> (a, b and f, g) and the corresponding element maps (c-e) and (h-j). EDS analysis results (mol%) were collected at the indicated spots (yellow dots) in graphs e and j. The catalyst was cooled to room temperature in a lean feed after aging.

catalysts because of the peak shift to lower bond length comparing to that in 0.5Rh/Al<sub>2</sub>O<sub>3</sub>. To understand the difference in Rh coordination structures, the EXAFS fitting results for Rh K-edge in the first coordination shell are shown in Table S4. The CN of Rh-O bond decreases with increasing Pt: 0.5Rh/Al<sub>2</sub>O<sub>3</sub> (5.6) > 1Pt-0.5Rh/Al<sub>2</sub>O<sub>3</sub> (5.2) > 2Pt-0.5Rh/Al<sub>2</sub>O<sub>3</sub> (4.8), which is consistent with the trend for Rh oxidation state

(Table S3). These results further demonstrate the mutual influence between Pt and Rh on Pt-Rh catalysts in terms of physical state of metals and their electronic structures.

There appears to be an apparent inconsistency in oxidation state measured by XANES and by XPS, especially for Pt. This can be explained by the difference between these two techniques. XAS (EXAFS and

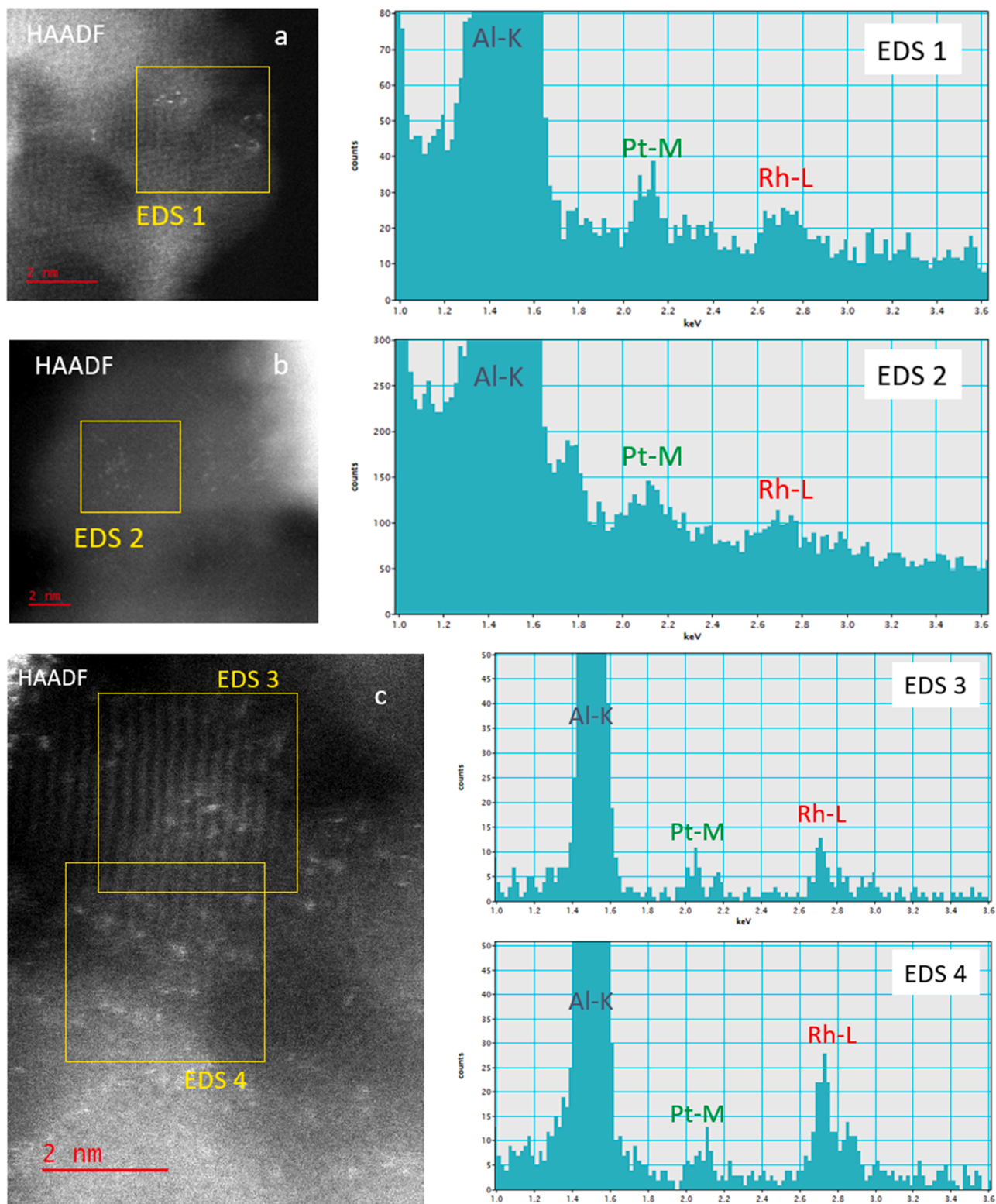


**Fig. 5.** EDS spectra of aged 2Pt-0.5Rh/Al<sub>2</sub>O<sub>3</sub> collected in areas where no obvious nanoparticles observed.

XANES) is a bulk technique, and its signal is volume averaged. The oxidation state obtained by XANES reflects the averaged oxidation state of all metal species. XPS on the other hand is a surface technique, which detects only the surface species (typically a few nm). Combining both techniques, we can come to the conclusion that the bulk of Pt particles is metallic but its surface is partially oxidized. XANES measurements on the Rh-containing catalysts also include Rh aluminate species that could

be buried beneath the surface and not detectable by XPS. As a result, the average oxidation states of Rh obtained by XANES are higher than those obtained by XPS. Nevertheless, the results from both techniques show the same trend, i.e., the presence of Pt makes Rh more metallic.

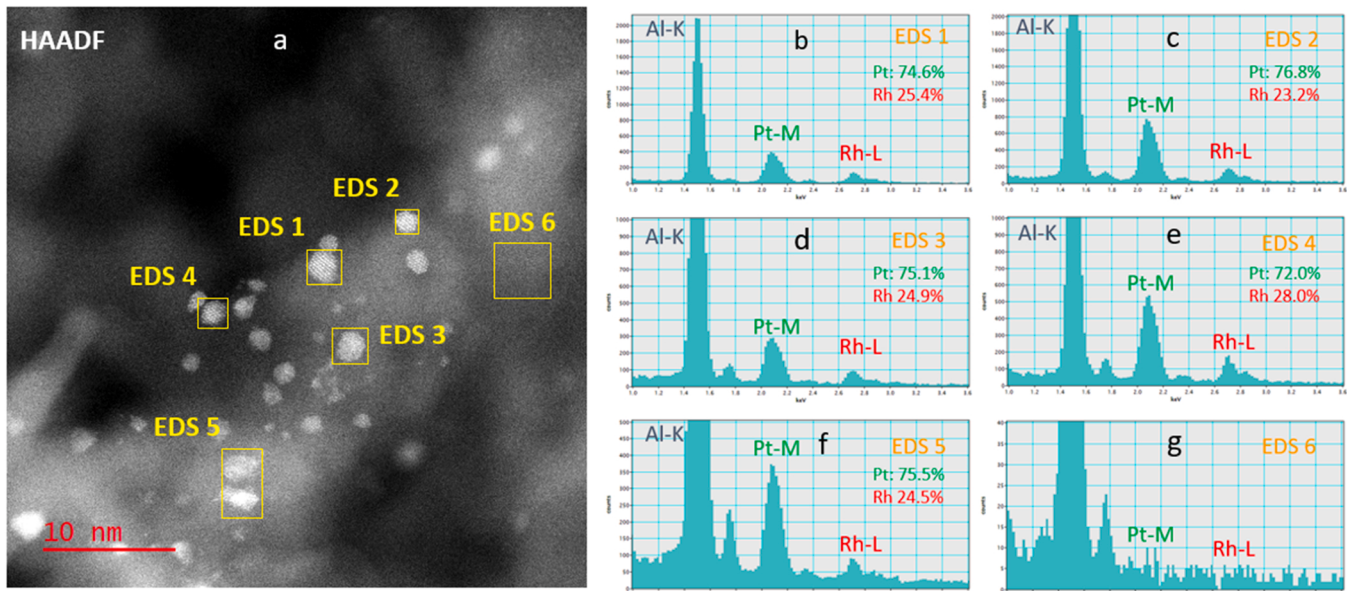


**Fig. 6.** AC-STEM image of fresh (calcined at 550 °C for 2 h) 2Pt-0.5Rh/Al<sub>2</sub>O<sub>3</sub> (a) and EDS spectra of highlighted areas (b-g). Pt and Rh concentrations (mol%) in (b) to (f) are from the integrated EDS spectra of the indicated areas in (a).

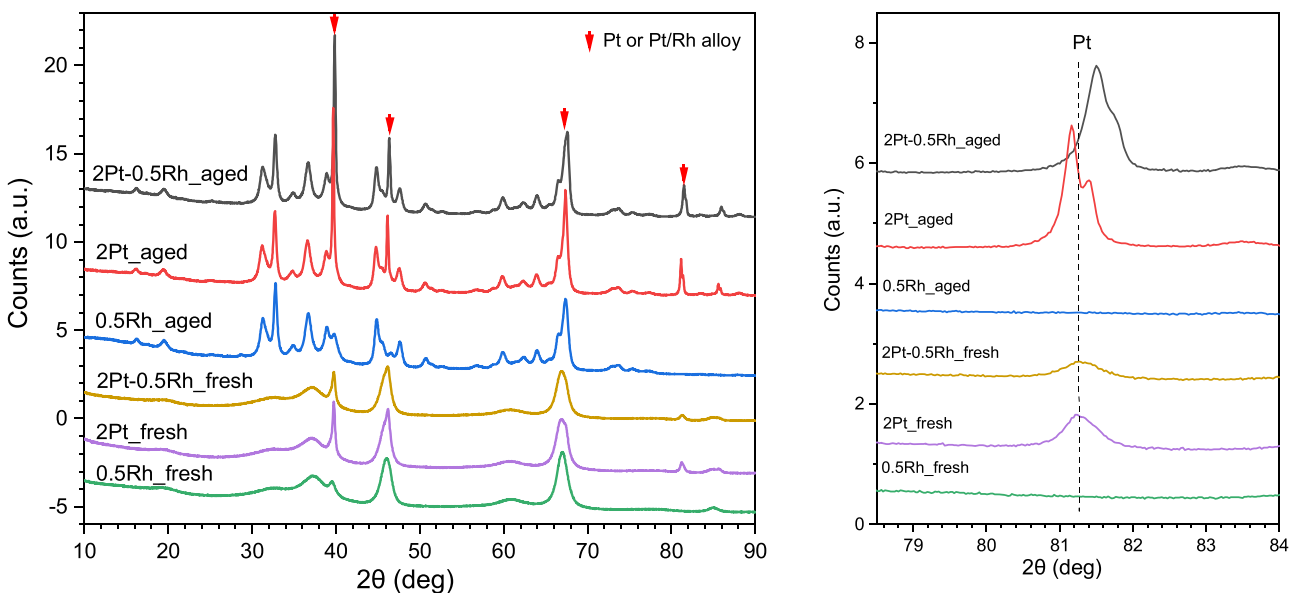


**Fig. 7.** XRD scans of fresh and aged 0.5Rh, 2Pt and 2Pt-0.5Rh catalysts (A) and their detailed view of Pt or Pt/Rh alloy peak between 79° and 83° (2θ) (B).

### 3.3. The origin of Pt-Rh synergy

To understand the origin of Pt-Rh synergy, it is helpful to discuss the characteristics of the monometallic catalysts first. Intrinsically, Pt is much less active than Rh for TWC. On fresh catalysts, where both Pt and Rh are highly dispersed, the T50s for CO, NO and HC on 2 % Pt/Al<sub>2</sub>O<sub>3</sub> are 54, 77 and 65 °C higher than those on 0.5 % Rh/Al<sub>2</sub>O<sub>3</sub> (Fig. S4). The poor low-temperature activity of Pt has been extensively reported for NO reduction by CO under stoichiometric feed conditions and was related to the CO inhibition effect [10–12]. Due to its strong binding energy [26], CO strongly adsorbs on Pt surface at low temperatures to the extent preventing the access to the surface by O<sub>2</sub> and NO. Thus, a higher temperature is needed to desorb the strongly adsorbed CO and allow the reaction to occur. On the other hand, CO adsorbs on Rh less strongly than Pt, and NO adsorption and dissociation are more favored

on Rh [11,12]. This activity disparity becomes even more pronounced under engine exhaust conditions, where the CO concentration is about an order of magnitude higher than NO.

Catalyst aging behavior is particularly important to the applications of TWC catalysts and a focus for this work. Pt is vulnerable to sinter under high-temperature aging conditions, especially in an O<sub>2</sub>-rich environment. The Pt dispersion on the Pt/Al<sub>2</sub>O<sub>3</sub> reference catalysts was reduced to about 1 % after aging at 1050 °C in a lean/rich feed (Table 2). The severity of Pt sintering on 2% Pt/Al<sub>2</sub>O<sub>3</sub> is further evidenced by the SEM results. Not surprisingly, the aged Pt catalysts are by far the least active catalysts. Rh on the other hand has a different aging behavior on an Al<sub>2</sub>O<sub>3</sub> support. On all the TEM images collected, we did not observe any Rh particles on the aged 0.5% Rh/Al<sub>2</sub>O<sub>3</sub> catalyst; but the EDS area mappings and spectra indicate a uniform distribution of Rh on the support (Fig. 3). This suggests that the Rh species may exist as sub-

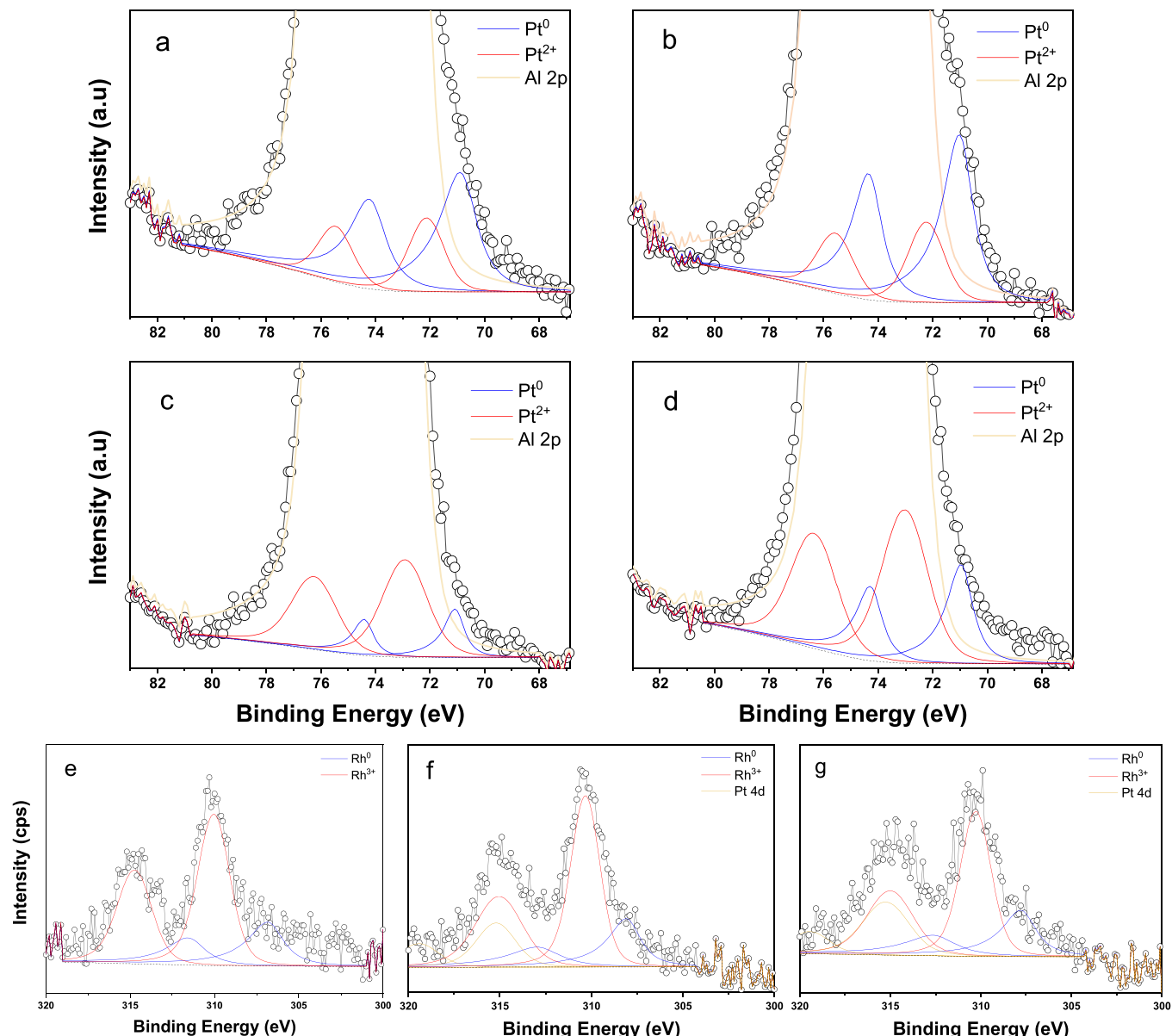


**Fig. 8.** XPS Pt 4f spectra for aged 1Pt (a), 2Pt (b), 1Pt-0.5Rh (c) and 2Pt-0.5Rh (d) and Rh 3d spectra for aged 0.5Rh (e), 1Pt-0.5Rh (f) and 2Pt-0.5Rh (g).

nanometer moieties on or in the  $\text{Al}_2\text{O}_3$  support. This conclusion is consistent with the XRD results; no Rh diffraction peaks were found (Fig. 7). In contrast to Pt, under high-temperature lean conditions, Rh species on an alumina support can be severely deactivated due to strong-metal support interaction, to the extent forming inactive compounds. The deactivated Rh species can only be partially recovered after a reduction treatment [13–17]. The absence of Rh particles in the TEM and XRD results, the low specific CO uptake in the CO chemisorption measurements, as well as the detection of Rh-O-Al linkage by the EXAFS experiment suggest that a part of Rh sites on the aged Rh catalyst may have formed inactive Rh species under our aging condition.

Because of the vulnerability of Pt to aging and its low intrinsic activity, on an aged Pt-Rh catalyst, Rh should have a dominant contribution to the overall kinetics at low temperatures. Therefore, understanding the change of Rh should be key to revealing the origin of Pt-Rh synergism. The XPS results indicate that the surface Rh concentrations on a Pt-Rh catalyst is significantly higher than that on the Rh reference. Similarly, both CO chemisorption and CO-DRIFTS data show that the number of active surface Rh sites, capable of adsorbing CO, is

much higher on a Pt-Rh catalyst than on the Rh reference. The physical states of Rh sites on aged Pt-Rh catalysts can be directly visualized on the AC-STEM/EDS images (Fig. 4). In addition to the highly dispersed, sub-nanometer Rh species on the  $\text{Al}_2\text{O}_3$  support, Rh nanoparticles and islands are found on large Pt particles. The Pt-bound Rh species not only increase the number of active Rh sites; these Rh species, based on XPS and XANES results, are more metallic relative to the Rh reference. A more reduced Rh catalyst is known to be more active for TWC catalysis. Therefore, the creation of the additional, more active Rh sites on the aged Pt-Rh catalysts should be the main reason for the Pt-Rh synergy.

All our experimental evidence indicates that the direct contact between Rh and Pt is key to the observed Pt-Rh synergistic effect. To support this point, we have conducted an experiment to compare the activities of aged 2Pt-0.5Rh and those of a physical mixture of aged Pt and Rh catalysts, both having identical overall composition and sample weight. As shown in Fig. S5, the light-off temperatures of 2Pt-0.5Rh are significantly lower than those of the mixture catalyst (by 31, 39 and 50 °C for CO, NO and HC, respectively). These results further illustrate that Pt-Rh synergism requires close proximity between these two metals.

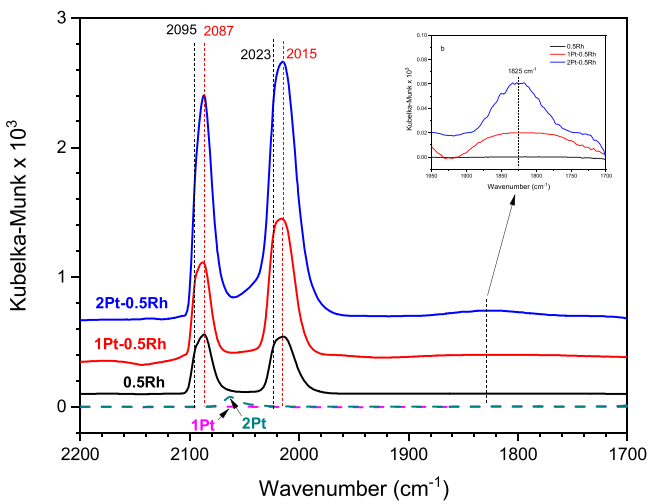


**Fig. 9.** CO-DRIFTS results on aged 1Pt, 2Pt, 0.5Rh, 1Pt-0.5Rh and 2Pt-0.5Rh. The inserted graph is a zoomed view between 1700 and  $1950\text{ cm}^{-1}$ .

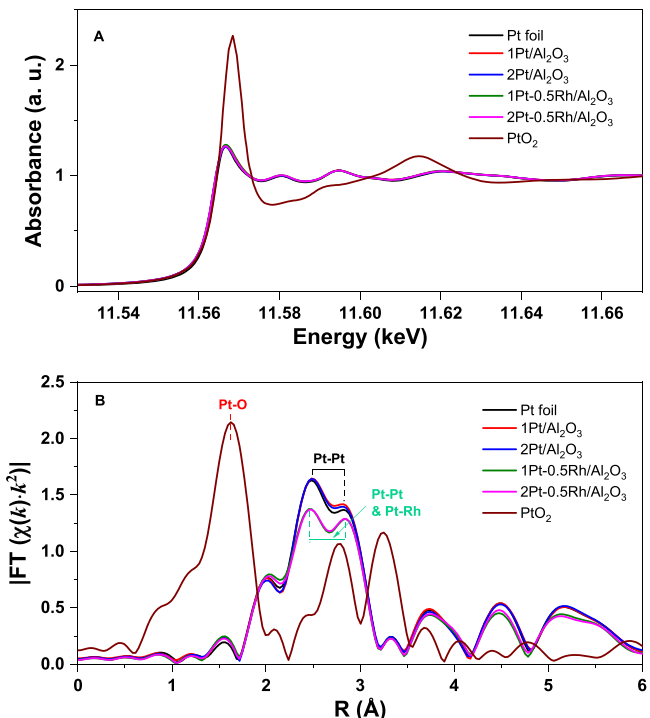


**Fig. 10.** Structural characterization. (A) Normalized Pt L<sub>3</sub>-edge XANES and (B) Fourier transformed  $k^2$ -weighted EXAFS oscillations in R space for Pt L<sub>3</sub>-edge in aged 1Pt/ $\text{Al}_2\text{O}_3$ , 2Pt/ $\text{Al}_2\text{O}_3$ , 1Pt-0.5Rh/ $\text{Al}_2\text{O}_3$ , and 2Pt-0.5Rh/ $\text{Al}_2\text{O}_3$  catalysts.

Our XRD results indicate that there is a certain degree of alloy formation on aged 2Pt-0.5Rh. The slightly lower Pt-Pt coordination number on 2Pt-0.5Rh (10.4) than that of 2Pt (11.4) as well as a low degree of Pt-Rh coordination (0.7) obtained from EXAFS indicate the presence of a limited Pt-Rh bonding in 2Pt-0.5Rh. Combining these structure characterizations with the AC-STEM results, we think that a likely structure of the bimetallic particles could involve surface bonding of small Rh<sub>x</sub>O<sub>y</sub> species with Pt surfaces. The environment during our cooling step after aging is entirely oxidizing, which makes it less likely to maintain a homogeneous alloy phase.

Bulk Pt/Rh alloys were reported to form in a continuously reducing environment, such as H<sub>2</sub>, at elevated temperatures. However, a homogeneous Pt-Rh alloy would undergo a phase segregation when exposed

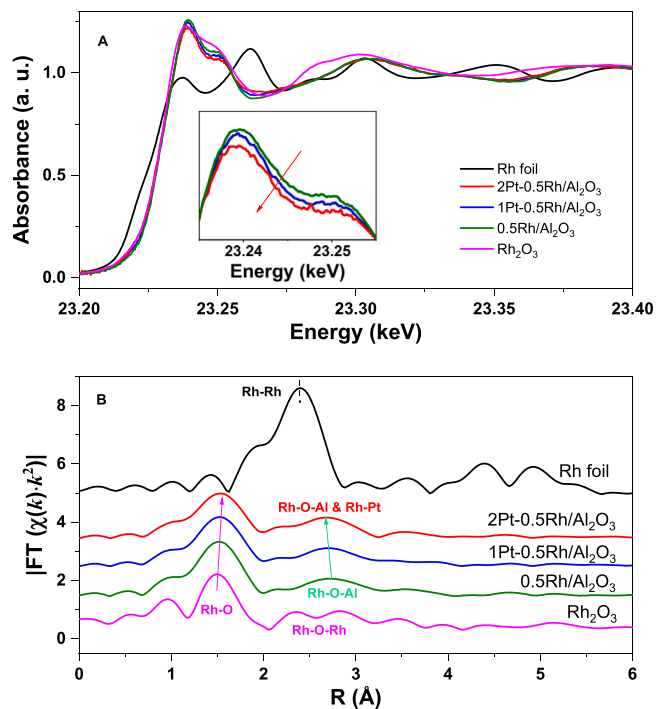


**Fig. 11.** Structural characterization. (A) Normalized Rh K-edge XANES and (B) Fourier transformed  $k^2$ -weighted EXAFS oscillations in R space for Rh K-edge in aged 0.5Rh/ $\text{Al}_2\text{O}_3$ , 1Pt-0.5Rh/ $\text{Al}_2\text{O}_3$ , and 2Pt-0.5Rh/ $\text{Al}_2\text{O}_3$  catalysts.

to O<sub>2</sub> or NO from the gas phase due to the formation of more stable Rh-O bond vs. Pt-O, resulting in a surface enrichment of Rh oxide [22,23, 27–29]. Thus, even if a homogeneous alloy was formed during our aging process, it would have been largely converted to heterogeneous bimetallic moieties during our oxidative cooling step. To test this hypothesis, we investigated the effect of cooling environment after aging. We aged one 2Pt-0.5Rh catalyst under our standard condition (1050 °C, 10% H<sub>2</sub>O, lean/rich) but cooled the catalyst to room temperature in a rich feed (4% H<sub>2</sub>/N<sub>2</sub>). In a separate experiment, we aged another 2Pt-0.5Rh catalyst in the same way and cooled in the same feed but only to 400 °C; at 400 °C the catalyst was re-oxidized in air for 1 h. The AC-STEM results of these two catalysts (Figs. S6 and S7) show that the metal particles on the first catalyst (cooled in rich feed) look more uniform with mostly Pt (>95 at% for spot analysis). On the second catalyst (with subsequent reoxidation), Rh species are clearly segregated out to the surface as small nanoparticles and islands. The surface enrichment is especially evident when looking along the edge of the large bimetallic particles.

To understand the temperature required to create this synergy, we also evaluated fresh (calcined at 550 °C in air for 2 h) and 800 °C lean/rich aged 2Pt, 0.5Rh and 2Pt-0.5Rh catalysts for TWC activity. Surprisingly, we observed a significant synergistic effect between Pt and Rh with both treatment conditions (Fig. S4). Even an oxidation treatment at 550 °C is sufficient to give rise to the Pt-Rh synergy. As shown by the AC-STEM results (Fig. 6), this fresh 2Pt-0.5Rh catalyst contains highly dispersed Pt/Rh particles (mostly <2 nm particles), which, according to our EDS analysis, attracts about 70 % Rh deposited on the catalyst. Interestingly, XRD scans detected only Pt diffractions, no alloy phase (Fig. 7B). XPS analysis of this fresh 2Pt-0.5Rh catalyst shows mixed valent states for Pt (64 % Pt<sup>0</sup>, 27 % Pt<sup>2+</sup>, 9 % Pt<sup>4+</sup>) and Rh (55 % Rh<sup>0</sup> and 45 % Rh<sup>3+</sup>). Therefore, Pt-Rh alloy formation is not a necessity for the Pt-Rh synergy; but their direct interaction must be required.

A close contact between Pt and Rh most certainly would facilitate the electronic interactions between the metals. The more reduced state of Rh on 2Pt-0.5Rh relative to 0.5Rh is believed to be the primary reason for its higher specific rate. A Rh catalyst has a low NO dissociation barrier. However, under reaction conditions strong O<sub>2</sub> adsorption and

dissociation on Rh sites cause surface poisoning by atomic O [30]. Rh sites connected to metallic Pt particles are more inducive to remove the adsorbed oxygen atoms through electron transfer from the electron-rich Pt particles and thereby attain higher activity at low temperatures. On the other hand, a secondary benefit from this interaction could come from the change of physical and electronic state of Pt. The XPS results (Table 2) show a higher surface Pt concentration and higher Pt oxidation state on the 2Pt-0.5Rh catalyst relative to the 2Pt reference. Rh in 2Pt-0.5Rh evidently reduces the sintering of Pt particles (SEM results) presumably by altering the surface tension of the metal particles through  $\text{RhO}_x$  decoration. These modified features of Pt can certainly help to reduce the CO inhibition effect on Pt at low temperatures and contribute to the improved TWC activity at high temperatures.

#### 4. Conclusions

We have conducted an extensive study on a series of  $\text{Al}_2\text{O}_3$  supported Pt, Rh and Pt-Rh catalysts for TWC catalysis as a function of Pt/Rh ratio, catalyst aging condition and test protocol. Profound synergy between Pt and Rh was observed on all Pt-Rh compositions investigated relative to their single metal references with significantly reduced light-off temperatures. The nature of this synergy was investigated using various characterization techniques, including CO chemisorption, SEM/EDS, TEM/EDS, AC-STEM/EDS, XRD, XPS, CO-DRIFTS, EXAFS and XANES. The CO chemisorption, CO-DRIFTS and XPS results show that the active surface Rh concentration on an aged Pt-Rh catalyst is much higher than that of the Rh reference, and the XPS and XANES experiments reveal that Rh on the bimetallic catalyst is more reduced. AC-STEM images and EDS mapping clearly illustrate that there are two types of Rh species on an aged Rh-Pt catalyst in terms of its location: one sitting on Pt particles as Rh nanoparticles and islands and the other closely associated with the alumina support as sub-nano or even atomically dispersed Rh or Rh-Al moieties. The Pt-Rh bimetallic particles contain a low degree of Pt-Rh alloy as evidenced by the upshift of the peaks associated with the metal diffraction and by a low degree of Pt-Rh coordination concluded from the EXAFS measurement. Combining all structural and microscopy analyses, we conclude that the Rh species on the Pt-Rh bimetallic particles is surface enriched, and this surface enrichment is driven by the interaction between Rh and  $\text{O}_2$  (during cooling after aging) or NO (during reaction). The primary contribution to the enhanced activity of the Pt-Rh catalyst comes from the Rh species sitting on the Pt particles, which has a lower oxidation state than that on the Rh/ $\text{Al}_2\text{O}_3$  reference due to Pt-Rh interaction.

#### CRediT authorship contribution statement

**Yuejin Li:** Conceptualization, Investigation – experiment planning and data analysis, Writing – original draft, Writing – review & editing. **Ke-Bin Low:** Investigation - microscopies, Writing – review & editing. **Andreas Sundermann:** Investigation – catalytic performance, Writing – review & editing. **Haiyang Zhu:** Investigation - FTIR, Writing – review & editing. **Luis E. Betancourt:** Investigation – XPS, Writing – review & editing. **Chansoon Kang:** Investigation – SEM. **Shantel Johnson:** Investigation - XRD. **Shaohua Xie:** Investigation – CO chemisorption and XAS. **Fudong Liu:** Investigation - CO chemisorption and XAS, data analysis, Writing - review & editing.

#### Declaration of Competing Interest

The authors declare that they have no known competing financial interests or personal relationships that could have appeared to influence the work reported in this paper.

#### Data availability

Data will be made available on request.

#### Acknowledgments

This work was supported by BASF Environmental Catalyst and Metal Solutions, and we thank BASF for permission to publish this work. F. L. sincerely thanks the research fund from BASF and the Startup Fund from the University of Central Florida (UCF). S. X. thanks the support from the Preeminent Postdoctoral Program (P3) at UCF. The AC-STEM experiment was performed using the instrument in the Electron Microscopy Core in the Research Resources Center of University of Illinois Chicago. The XAS experiment was conducted at the beamline 7-BM (QAS) of the National Synchrotron Light Source II, a U.S. Department of Energy (DOE) Office of Science User Facility operated for the DOE Office of Science by the Brookhaven National Laboratory under contract no. DE-SC0012704.

#### Appendix A. Supporting information

Supplementary data associated with this article can be found in the online version at doi:10.1016/j.apcatb.2023.122821.

#### References

- [1] R.J. Farrauto, M. Deeba, S. Alerasool, Gasoline automobile catalysis and its historical journey to cleaner air, *Nat. Catal.* 2 (2019) 603–613.
- [2] Y. Jing, G. Wang, S. Mine, J. Kawai, R. Toyoshima, H. Kondoh, X. Zhang, S. Nagaoka, K. Shimizu, T. Toyao, Promoting effect of basic metal additives on DeNOx reactions over Pt-based three-way catalysts, *J. Catal.* 416 (2022) 209–221.
- [3] Y.F. Chu, E. Ruckenstein, On the sintering of platinum on alumina model catalyst, *J. Catal.* 55 (1978) 281.
- [4] V. Matsouka, M. Konsolakis, I.V. Yentekakis, A. Papavasiliou, A. Tsetsekou, N. Boukos, Thermal aging behavior of Pt-only TWC converters under simulated exhaust conditions: effect of rare earths ( $\text{CeO}_2$ ,  $\text{La}_2\text{O}_3$ ) and alkali (Na) modifiers, *Top. Catal.* 54 (2011) 1124–1134.
- [5] H. Xiong, E.J. Peterson, G. Qi, A.K. Datye, Trapping mobile Pt species by Pd in diesel oxidation catalysts: smaller is better, *Catal. Today* 272 (2016) 80–86.
- [6] C. Carrillo, A. DeLaRiva, H. Xiong, E.J. Peterson, M.N. Spilde, D. Kunwar, R. S. Goeke, M. Wiebeng, S.H. Oh, G. Qi, S.R. Challa, A.K. Datye, Regenerative trapping: how Pd improves the durability of Pt diesel oxidation catalysts, *Appl. Catal. B: Environ.* 218 (2017) 581–590.
- [7] M. Ozawa, T. Okouchi, M. Haneda, Three way catalytic activity of thermally degenerated Pt/ $\text{Al}_2\text{O}_3$  and Pt/ $\text{CeO}_2\text{-ZrO}_2$  modified  $\text{Al}_2\text{O}_3$  model catalysts, *Catal. Today* 242 (2015) 329–337.
- [8] V. Matsouka, M. Konsolakis, L.V. Yentekakis, A. Papavasiliou, A. Tsetsekou, N. Boukos, Thermal aging behavior of Pt-only TWC converters under simulated exhaust conditions: effect of rare earths ( $\text{CeO}_2$ ,  $\text{La}_2\text{O}_3$ ) and alkali (Na) modifiers, *Top. Catal.* 54 (2011) 1124–1134.
- [9] A.G. v.d. Bosch-Driebergen, M.N.H. Kieboom, A.V. Dreumel, R.M. Wolf, F.C.M.J.M. v Delft, B.E. Nieuwenhuys, Reduction of nitric oxide by carbon monoxide over silica-supported platinum-rhodium alloys, comparison with  $\text{CO} + \text{O}_2$  reaction, *Catal. Lett.* 2 (1989) 235–242.
- [10] S.H. Oh, G.B. Fisher, J.E. Carpenter, D.W. Goodman, Comparative kinetic studies of  $\text{CO-O}_2$  and  $\text{CO-NO}$  reactions over single crystal and supported rhodium catalysts, *J. Catal.* 100 (1986) 360–376.
- [11] S.B. Schwartz, G.B. Fisher, L.D. Schmidt,  $\text{NO} + \text{CO}$  reaction on Rh (111): Steady-state rates and adsorbate coverages, *J. Phys. Chem.* 92 (1988) 389–395.
- [12] B.E. Nieuwenhuys, Adsorption and reactions of CO, NO,  $\text{H}_2$  and  $\text{O}_2$  on Group VIII metal surfaces, *Surf. Sci.* 126 (1983) 307.
- [13] Z. Weng-Sieh, R. Gronsky, A.T. Bell, Microstructural evolution of  $\gamma$ -alumina-supported Rh upon aging in air, *J. Catal.* 170 (1997) 62–74.
- [14] S. Suhonen, M. Valden, M. Hietikko, R. Laitinen, A. Savimäki, M. Häkkinen, Effect of Ce-Zr mixed oxides on the chemical state of Rh in alumina supported automotive exhaust catalysts studied by XPS and XRD, *Appl. Catal. A* 218 (2001) 151–160.
- [15] C. Li, J. Wu, A.B. Getsoian, G. Cavataio, J.R. Jinschek, Direct observation of rhodium aluminate ( $\text{RhAlO}_x$ ) and its role in deactivation and regeneration of Rh/ $\text{Al}_2\text{O}_3$  under three-way catalyst conditions, *Chem. Mater.* 34 (5) (2022) 2123–2132.
- [16] C. Wong, R. McCabe, Effect of high-temperature oxidation and reduction on the structure and activity of  $\text{RhAl}_2\text{O}_3$  and  $\text{RhSiO}_2$  catalysts, *J. Catal.* 119 (1989) 47–64.
- [17] M. Machida, Y. Uchida, S. Iwashita, H. Yoshida, M. Tsushima, J. Ohyama, Y. Nagao, Y. Endo, T. Wakabayashi, Catalyst deactivation via rhodium-support interactions under high-temperature oxidizing conditions: a comparative study on hexaaluminates versus  $\text{Al}_2\text{O}_3$ , *ACS Catal.* 11 (15) (2021) 9462–9470.
- [18] V.O. Stoyanovskii, A.A. Vedyagin, A.M. Volodin, R.M. Kenzhin, Y.V. Shubin, P. E. Plyusnin, I.V. Mishakov, Peculiarity of Rh bulk diffusion in La-doped alumina and its impact on CO oxidation over Rh/ $\text{Al}_2\text{O}_3$ , *J. Catal. Comm.* 97 (2017) 18–22.
- [19] S.H. Oh, J.E. Carpenter, Platinum-rhodium synergism in three-way automotive catalysts, *J. Catal.* 98 (1986) 178–190.

- [20] Z. Hu, F.M. Allen, C.Z. Wan, R.M. Heck, J.J. Steger, R.E. Lakis, C.E. Lyman, Performance and structure of Pt-Rh three-way catalysts: mechanism for Pt/Rh synergism, *J. Catal.* 174 (1998) 13–21.
- [21] R. Polvinen, M. Vippola, M. Valden, T. Lepistö, A. Suopanki, M. Härkönen, The effect of Pt-Rh synergism on the thermal stability of rhodium oxide on pure alumina and Ce-ZrO<sub>2</sub>-modified alumina-supported catalysts, *J. Catal.* 226 (2004) 372–381.
- [22] R.E. Larkis, Y. Cai, H.G. Steger Jr., C.E. Lyman, Alumina-supported Pt-Rh catalysts, II. Kinetic characterization and synergistic effects, *J. Catal.* 154 (1995) 276–287.
- [23] A. Bosch-Driebergen, M. Kieboom, A. Dreumel, R. Wolf, F. Delft, B. Nieuwenhuys, CO oxidation over silica supported Pt-Rh alloy catalysts, *Catal. Lett.* 2 (1989) 73.
- [24] L. Heezen, V.N. Kilian, R.F. van Slooten, R.M. Wolf, B.E. Nieuwenhuys, NO reduction and adsorption intermediates on Pt-Rh alloy catalysts, in: A. Crucq (Ed.), *Catalysis and Automotive Pollution Control II*, Elsevier Science Publishers B.V., Amsterdam, 1991, pp. 381–393.
- [25] A. Sundermann, O. Gerlach, High-throughput screening as a supplemental tool for the development of advanced emission control catalysts: methodological approaches and data processing, *Catalysts* 6 (2) (2016) 23, <https://doi.org/10.3390/catal6020023>.
- [26] R.F. van Slooten, B.E. Nieuwenhuys, An infrared study of the interaction of CO and NO with a silica supported Pt-Rh alloy catalyst, *J. Catal.* 122 (1990) 429–437.
- [27] T. Wang, L.D. Schmidt, Surface enrichment of Pt-Rh alloy particles by oxidation-reduction cycling, *J. Catal.* 71 (1981) 411–422.
- [28] F.C.M.J.M. v. Delft, J. Siera, B.E. Nieuwenhuys, The transient behaviour of Pt-Rh (410) alloy surfaces upon interaction with O<sub>2</sub>, NO and CO, *Surf. Sci.* 208 (1989) 365–382.
- [29] Y. Matsumoto, Y. Aibara, K. Mukai, K. Moriwaki, Y. Okawa, B.E. Nieuwenhuys, K. Tanaka, STM studies of oxygen-induced reconstruction alloy surface on a Pt-Rh (100), *Surf. Sci.* 377–379 (1997) 32–37.
- [30] M.W. Lee, E.J. Lee, K.-Y. Lee, Comparative analysis of NO<sub>x</sub> reduction on Pt, Pd, and Rh catalysts by DFT calculation and microkinetic modeling, *Appl. Surf. Sci.* 611 (2023), 155572.